Uniformly electrodeposited α-MnO_2 film on super-aligned electrospun carbon nanofibers as a bifunctional catalyst for the oxygen reduction reaction

By: Zheng Zeng, Wendi Zhang, Yiyang Liu, Pei Lu, and Jianjun Wei

Z. Zeng, W. Zhang, Y. Liu, P. Li, J. Wei, Uniformly electrodeposited α-MnO_2 film on super-aligned electrospun carbon nanofibers as a bifunctional catalyst for the oxygen reduction reaction, *Electrochimica Acta*, **2017**, 256, 232-240, http://www.doi.org/10.1016/j.electacta.2017.10.057.

Abstract:

Metal oxide/carbonaceous nanomaterials are promising candidates for the oxygen reduction in energy converting systems. However, inhomogeneous surface coverage allows hydrogen peroxide to escape into the bulk solution due to unstable metal or metal oxide/carbonaceous nanomaterial synthesis, which limits their performance in fuel cells. Here, we show that the above problems can be mitigated through a stable low-current electrodeposition of MnO_2 on super-aligned electrospun carbon nanofibers (ECNFs). The key to our approach is coupling a self-designed four steel poles collector for aligned ECNFs and a constant low-current (45 μA) electrodeposition technique for 4 h to form a uniform Na^+ induced α-MnO_2 film. By using the cyclic voltammetry to proceed the electrocatalytic oxygen reduction reaction (ORR), the bifunctional catalysts show a 3.84-electron pathway due to the rapid decomposition of hydrogen peroxide by the uniform α-MnO2 film and ending with formation of water. This research may enable a practical catalyst with a large number of cycling of oxygen reduction/regeneration to reduce the risk of the fuel cell degradation and an effective confinement of oxygen and hydrogen peroxide in the catalyst matrix to maximize the energy output of the fuel cell.

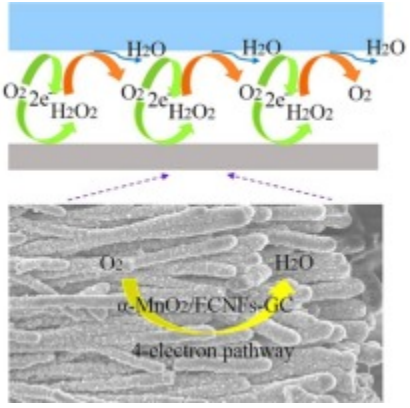

Keywords: MnO_2 | Electrospun carbon nanofibers | Bifunctional catalyst | Oxygen reduction reaction | Fuel cells

Article:

1. Introduction

A fuel cell has been one of the promising energy devices for generating clean and sustainable energy. Since the oxygen reduction reaction (ORR) is the most important reaction in energy converting systems such as proton exchange membrane (PEM) fuel cells, techniques used in electrocatalytic ORR studies have been widely developed [1], [2], [3], such as steady-state polarization [4], rotating disk electrode (RDE) [5], rotating ring-disk electrode (RRDE) [6], and cyclic voltammetry [7]. ORR in aqueous solutions undergoes mainly by two pathways: a 2-electron pathway from oxygen to hydrogen peroxide, and a 4-electron pathway from oxygen to water [3]. In order to ensure that the fuel cell generates the maximum power output, a 4-electorn pathway is necessary because the 2-electron pathway involved in the cathodic process seriously compromises the energy yield of the fuel cell [8], [9]. Moreover, the cell membranes and other supporting materials will be impaired in the presence of an excess hydrogen peroxide due to the peroxide radical formation generated from a disproportionation reaction [10], [11].

In the search of catalysts for limiting the hydrogen peroxide generation or decomposing generated hydrogen peroxide, carbon-based materials (glassy carbon (GC) [11], graphite [12], active carbon [13], and carbon nanotubes[14]), Pt catalysts (Pt electrode[15] and Pt alloys[16]), various porous materials [17], [18], [19], [20], and transition metal-based catalyst (cobalt[21] and iron[22]) have been greatly reported. The ORR performance of these metal-carbon catalysts varies with synthesis conditions, such as nitrogen type, metal type, and pyrolysis temperature [23]. In terms of number-electron pathway of ORR, 3.45 and 3.70 have been reported by using the catalysts of hematite nanoparticles supported on carbon nanotubes[24] or GC[8]. Although the confinement of oxygen within the catalysts is effective, inhomogeneous surface coverage allows hydrogen peroxide to escape into the bulk solution, which decreases the decomposition efficiency of generated hydrogen peroxide. Hence, a study to achieve stable synthesis of catalysts may lead to better strategies for achieving a 4-electron pathway.

Manganese dioxide (MnO_2) has been demonstrated to be one of the most promising catalyst materials for ORR, with a high electrocatalytic activity, ecofriendly properties, and abundant earth reserves [25], [26]. MnO_2 can exhibit diverse structures and polymorphs with the order of δ-MnO_2 < β-MnO_2 < amorphous MnO_2 < α-MnO_2 in ORR catalytic activity [27], [28]. Their ORR activity enhancement has been reported by introducing nitrogen-doping, oxygen vacancies, hydrogenation, metal-ion doping [29], [30], [31], [32], etc. More importantly, the catalytic decomposition of hydrogen peroxide by MnO_2 with high catalytic efficiency has been examined [33], [34]. However, a uniform MnO_2 film focusing on stable confinement of hydrogen peroxide for decomposing has not been achieved.

Carbon nanofibers (CNFs) are well known for their inexpensive production, freestanding nature, large porosity, and high conductivity as substrate materials [35], [36]. Electrospinning, which uses electric force to draw charged threads of polymer solutions or polymer melts into

nanofibers, has become an efficient fiber production method for creating porous electrospun CNFs (ECNFs) with a subsequent carbonization [37]. The nitrogen-doped ECNFs by carbonizing electrospun polyacrylonitrile (PAN) could be an electrocatalyst for ORR [38], [39]. In addition, aligned ECNF structures can be used as scaffolds to uniformly support metal oxide nano-architectures because their alignment can significantly enhance the deposition rate by shortening the distance of electron transport.

We hypothesize that the combination of these two materials (MnO_2 and super-aligned ECNFs) in a nanoscale structure will exhibit superior electrocatalytic, electrochemical, and mechanical properties for ORR catalytic activity. In this study, we describe the rational design and fabrication of MnO_2/ECNFs by wrapping MnO_2 onto super-aligned ECNFs. The nanocomposite of MnO_2/ECNFs is well-characterized. The as-prepared MnO_2/ECNFs-GC electrocatalytic system (electrodeposition of 4 h at 45 μA) exhibits a 3.84-electron pathway near the theoretical limit with a desirable confinement ability for both oxygen and hydrogen peroxide.

2. Experimental

2.1. Super-aligned ECNFs fabrication

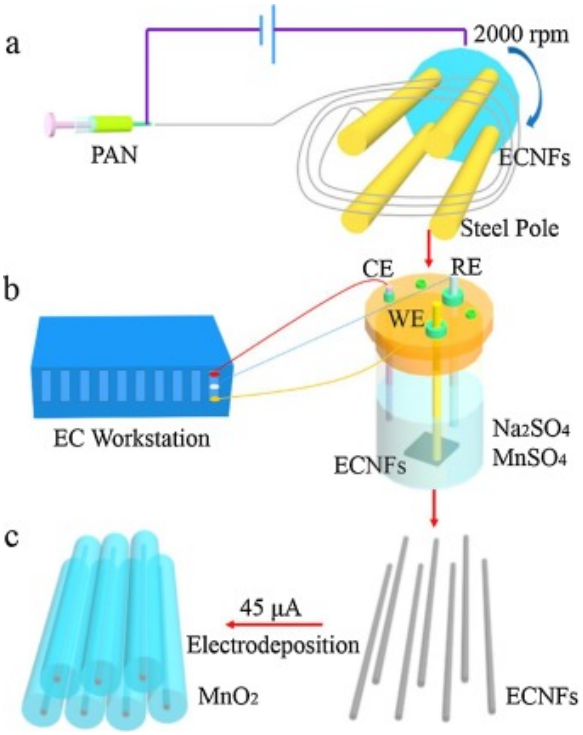

Fig. 1. (a) Illustrations of the electrospinning technique for the super-aligned ECNFs fabrication, (b) uniform electrodeposition of MnO_2 on the super-aligned ECNFs using a three-electrode setup with a ECNF mat working electrode, an Ag/AgCl reference electrode, and a platinum counter electrode, and (c) stable MnO_2 film formation after a uniform electrodeposition of 4 h.

The fabrication technique for the super-aligned ECNFs is schematically illustrated in Fig. 1a. A facile electrospinning method was used with a self-designed sample collector. Different from a normal cylinder design, four steel poles were welded on a plate in order to collect the ECNFs

without any substrates. A 10 wt.% polyacrylonitrile (PAN, MW = 150,000, ACROS Organics) solution in dimethylformamide (ACROS Organics) was electrospun onto the collector. The applied positive voltage was 18 kV and the distance between the needle tip and the collector was 15 cm. The collector was maintaining at a rate of 2000 revolutions per minute (rpm) during the electrospinning to form the super-aligned precursors. The obtained PAN sheets were then put into a furnace (Oxidation and Annealing Furnace) for stabilization to ensure that the fibers did not melt during pyrolysis. The heating rate was 1 °C/min from room temperature to 280 °C and kept for 6 h. The as-stabilized nanofibers were finally carbonized at 1200 °C for 1 h at a heating rate of 5 °C/min under N_2 atmosphere to yield high mechanical strength ECNFs.

2.2. MnO_2 electrodeposition on ECNFs

After the super-aligned ECNFs were prepared, MnO_2 was electrodeposited onto 1 cm^2 ECNFs with a three-electrode setup using a charging current of 45 μA performed on a bio-logic VMP3 electrochemical workstation (Fig. 1b). Here, a gold electrode taped with ECNFs, a platinum wire, and an Ag/AgCl were used as the working electrode, the counter electrode, and the reference electrode (Fisher Scientific), respectively. To assure that the deposition of MnO_2 took place uniformly and firmly at the ECNFs' surfaces (Fig. 1c), the ECNFs electrode was prior-treated with 4 M HNO_3 (J.T. Baker) solution at 70 °C for 2 h to introduce —OH and —COOH groups to facilitate the deposition. An aqueous precursor solution containing 10 mM $MnSO_4$ (ACROS Organics) and 100 mM Na_2SO_4 (ACROS Organics) was used as the supporting electrolyte. After the deposition, the working electrodes were washed with deionized water and then dried at 80 °C for 3 h.

2.3. Characterization

Field emission scanning electron microscope (FESEM) (Carl Zeiss Auriga-BU FIB FESEM Microscope) was performed to study the morphological properties of super-aligned ECNFs and MnO_2/ECNFs. Energy-dispersive X-ray spectroscopy (EDX) (Hitachi S-4800-I FESEM w/Backscattered Detector & EDX) and thermogravimetric analysis (TGA) (SDT Q600) were performed to study the atomic ratio of Mn: O and weight ratio of MnO_2 on MnO_2/ECNFs. Raman spectroscopy (Horiba XploRA One Raman Confocal Microscope System), Fourier transform infrared spectroscopy (FTIR) (Varian 670), and X-ray photoelectron spectroscopy (XPS, Thermo Fisher ESCALAB 250 Xi), were employed to study element components of MnO_2/ECNFs. X-ray powder diffraction (XRD) (Agilent Technologies Oxford Germini X-Ray Diffractometer) was employed to study the crystal structures of MnO_2/ECNFs.

2.4. Electrochemical study

Electrochemical performance was performed on a bio-logic VMP3 electrochemical workstation using a three-electrode testing system with a 3 mm diameter GC as the working electrode, a platinum wire as the counter electrode and an Ag/AgCl as the reference electrode (Fisher Scientific) in a 20 mM KCl (Sigma-Aldrich) electrolyte solution that was thoroughly degassed with O_2 gas. Usually acidic electrolytes are used in platinum or its alloys catalytic systems, which give high measured catalytic activity and help to conduct 4-electron ORR process [40]. However, acidic electrolytes are corrosive to fuel cell electrode materials. In addition, biological

full cells are operated at physiological pH and Cl^- is one of the most common anions presented in surface water [8]. Hence, in this work the benign neutral chloride solution is chosen on purpose to conduct the catalytic activity of MnO_2/ECNFs in ORR process. The super-aligned ECNFs and MnO_2/ECNFs were cut as 3 mm diameter wafers and then taped onto the GC using the conductive carbon glue (TED PELLA, INC) (Fig. S1) as modified electrodes for the electrochemical analysis of electro-reduction of oxygen. Cyclic voltammetry was then carried out after the modified GC electrode being immersed in a N_2 saturated 20 mM KCl solution for 15 min. Cyclic voltammetry was carried out at different scan rates (20, 40, 60, 80, 100, 150, and 200 mV/s) with a potential window between −1.0 V and 0.9 V.

3. Results and discussion

3.1. Characterization

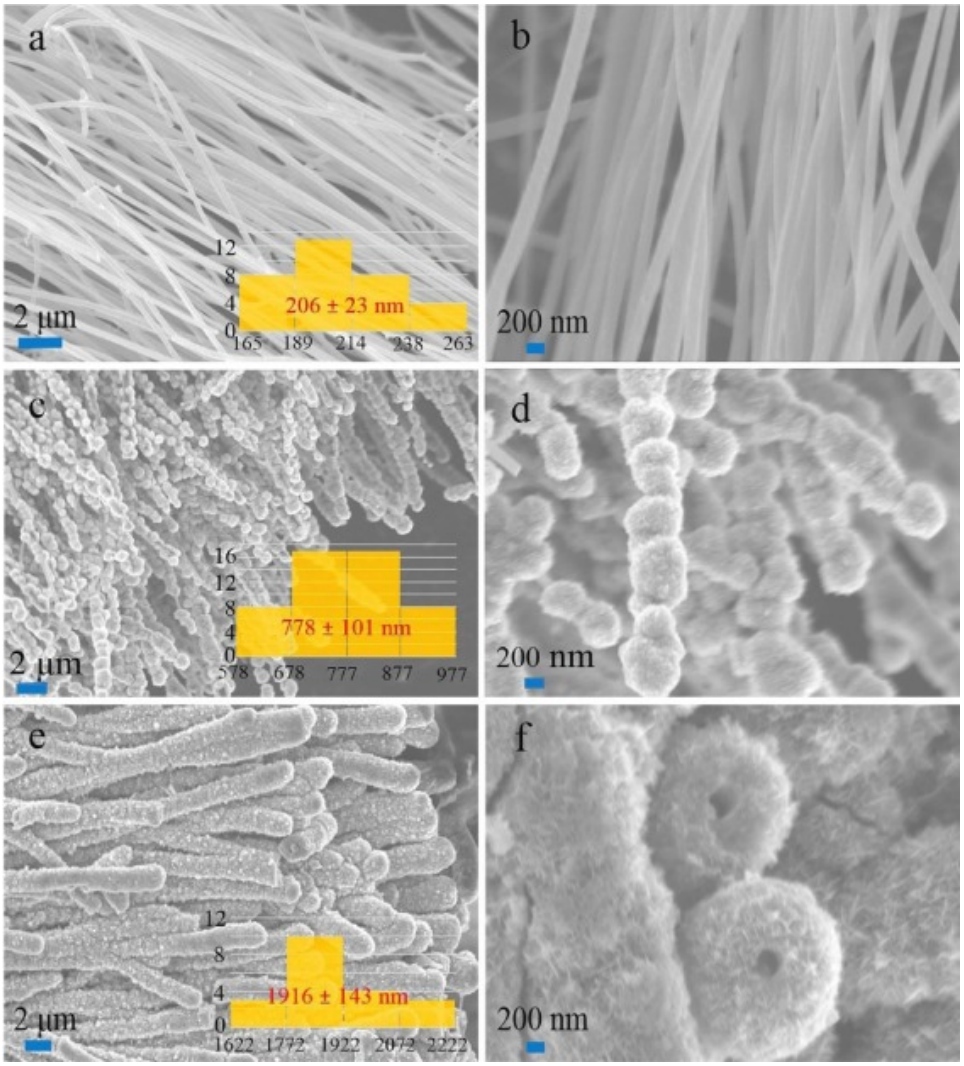

Fig. 2. SEM images of super-aligned ECNFs and MnO_2/ECNFs (electrodeposition for 2 h and 4 h) with the histograms of size distribution analysis. Note that b, d and f are enlarged images.

The as-prepared pure ECNFs exhibit super-aligned structure (Fig. 2a and b). It is hypothesized that the alignment of ECNFs can reduce the disordered electron flow, leading to a more uniform electrodeposition process by introducing reaction sites for nucleation of MnO_2 crystallites. MnO_2 was electrodeposited onto the ECNFs with a three-electrode setup (Fig. 1b). After electrodeposition for 2 h, small balls around the ECNFs present as the "kebab"-like structures. Although the SEM images clearly show surface structures corresponding to these firmly merged balls (Fig. 2c and 2d), the fibers are not fully covered. After electrodeposition for 4 h, the ECNFs with nanofiber diameter of about 206 nm are decorated by a MnO_2 film with a thickness of about 1710 nm, making a total diameter of ~1916 nm (Fig. 2e and 2f). These data corroborate the inference that the ECNFs' alignment promotes the homogenous electron flow and facilitates the uniform MnO_2 growth.

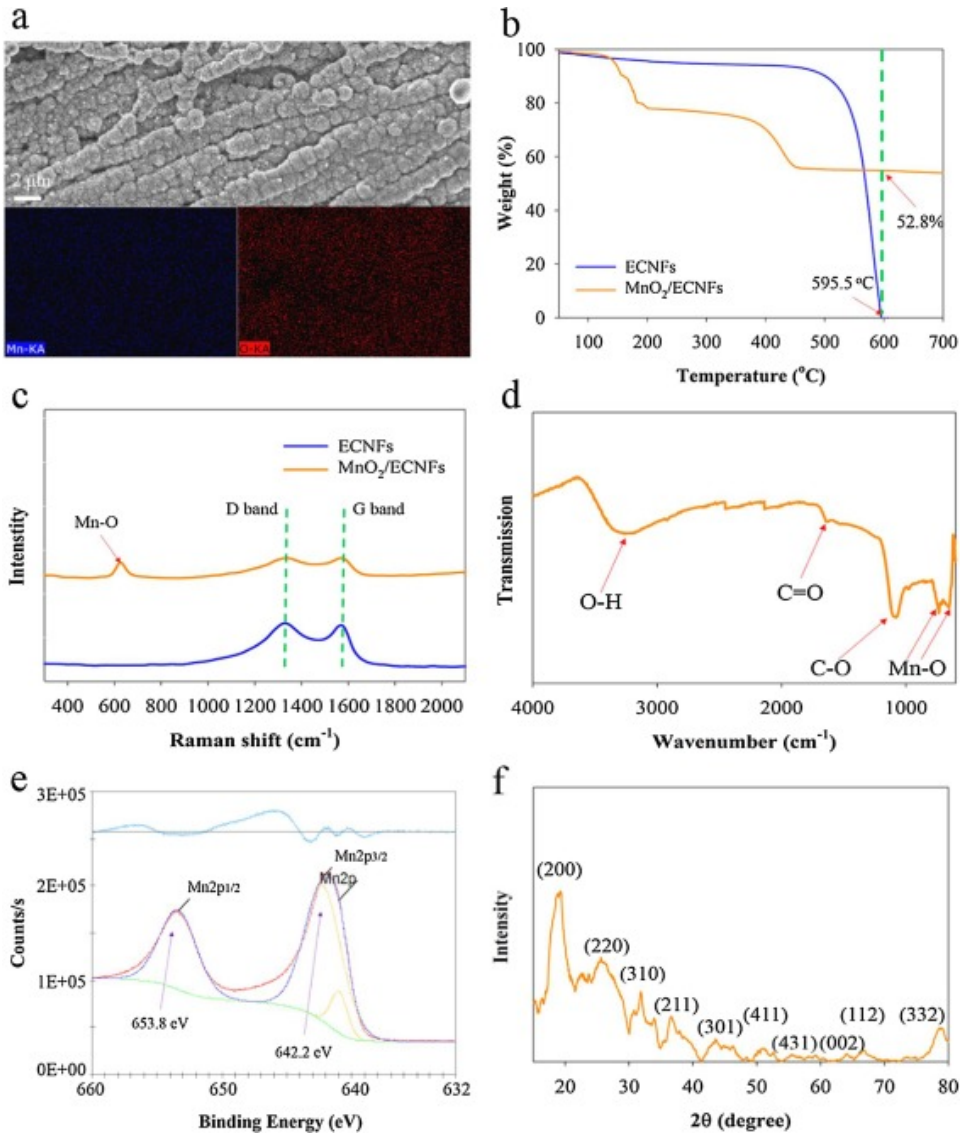

Fig. 3. The super-aligned ECNFs and MnO_2/ECNFs (4 h) are characterized using different techniques: (a) SEM associated with EDX mapping analysis, (b) TGA analysis, (c) Raman spectrum, (d) FTIR spectrum, (e) XPS spectrum, (f) XRD analysis.

The composites by 4 h electrodeposition were further analyzed by different kinds of techniques. EDX spectrum (Fig. 3a, Fig. S2) shows the surface composition is composed of the elements O and Mn. The atomic ratio of O and Mn is close to 2:1, which implies the formation of MnO_2. TGA of ECNFs and MnO_2/ECNFs to 700 °C in air was shown in Fig. 3b. Due to the residue solvent evaporation, the ECNFs sample shows a weight loss before 425.0 °C. And then the ECNFs sample decomposes until 595.5 °C. Unlike ECNFs, the MnO_2/ECNFs still achieve about 52.8% after 595.5 °C, indicating the weight fraction of MnO_2 on the MnO_2/ECNFs sample is about 52.8%. The success of MnO_2 deposition was further confirmed with Raman spectra and FTIR spectra. At Raman shift of 1325 cm^{-1} and 1569 cm^{-1}, the ECNFs sample shows D-band and G-band, respectively [41]. While, for the MnO_2/ECNFs sample, Mn-O presents at the Raman shift of 624 cm^{-1} (Fig. 3c) [37]. Correspondingly, ν(Mn-O) presents at the wavenumber of 643 cm^{-1} and 727 cm^{-1} according to the FTIR spectra (Fig. 3d). And IR transitions at 1176, 1647, and 3263 cm^{-1} are assigned to ν(C-O), ν(C═O), and ν(O-H), respectively [42], [43]. The chemical composition of the MnO_2/ECNFs sample was also investigated by the XPS. The high resolution Mn 2p spectra for MnO_2/ECNFs is presented in Fig. 3e. Two strong peaks at 642.2 and 653.8 eV can be clearly seen, [44] corresponding to the Mn $2p^{3/2}$ and Mn $2p^{1/2}$ spin–orbit peaks of MnO_2, respectively [45]. Furthermore, the crystal structures of the as-prepared MnO_2/ECNFs were also recorded by XRD (Fig. 3f), the patterns of which can be fully indexed to α-MnO_2 (JCPDS No. 44-0141) [46].

Herein, the excellent electrodeposition of MnO_2 originates from the stable structure of ECNFs, which contributes to a uniform Mn^{2+} flux. The electrochemical reaction occurs according to [47]:

$$Mn^2 + 2H_2O \rightarrow MnO_2 + 4H^+ + 2e^- \quad (1)$$

It is known that MnO_2 has different main structural motifs due to edge- or corner-sharing MnO_6 octahedra in different connectivity schemes, resulting in different tunnels extending in a direction parallel to the unit cell [28], [48]. In this study, the cations (Na^+) were introduced during the synthesis process, but the 1 × 1 tunnels (with a size of 0.189 nm) are generally too small for Na^+ to stabilize the structure, consequently resulting in the formation of α-MnO_2 due to structurally constructed from the double chains of edge-sharing MnO_6 octahedra which are linked at the corners to form 2 × 2 (with a size of 0.460 nm) and 1 × 1 tunnel structures [28], [48]. The crystal structure is confirmed by the XRD analysis of MnO_2/ECNFs by electrodeposition for 2 h (Fig. S3) and 4 h (Fig. 3f). Meanwhile, these cations inside 2 × 2 tunnels of α-MnO_2 increase the electronic conductivity of the MnO_2/ECNFs system, which indirectly enhance the electrodeposition of α-MnO_2 [49].

3.2. Catalytic properties

The ORR activity was firstly conducted by studying the cyclic voltammetric responses of a bare GC electrode as Fig. 4 shows. The cathodic peak results from the electrochemical reduction of oxygen and the magnitude of the cathodic peaks increases (Fig. 4a) with increasing of the voltage scan rates. In addition, the peak current, i_p (A), is measured as a function of the square root of the voltage scan rate (v (V/s)), which is found to exhibit a linear dependence (Fig. 4b). The dependence of the peak current position on the square root of the voltage scan rate for the bare GC electrode without modification can be firstly used to characterize the concentration of

oxygen in the bulk solution (C, mol/mL) through Randles-Sevcik equation (Note that the slope is obtained from the dependence of i_p (A) on v (V/s)) [50]:

$$|slope| = (2.99 \times 10^5) n^{3/2} \alpha^{1/2} A C D_0^{1/2} \quad (2)$$

where n is the number of electrons exchanged during the electrochemical process, α is the transfer coefficient (reported value of 0.26) [51], A is the active surface area of the bare GC electrode (0.071 cm^2), D_0 is the diffusion coefficient (reported value of 1.95×10^{-5} cm^2/s) [52]. Since the reduction of oxygen to hydrogen peroxide is known at the bare GC electrode, the number of electrons exchanged is 2 [53]. When the above constants are applied for absolute value of the slope obtained from Fig. 4b, the oxygen concentration of 3.11×10^{-7} mol/mL is extracted.

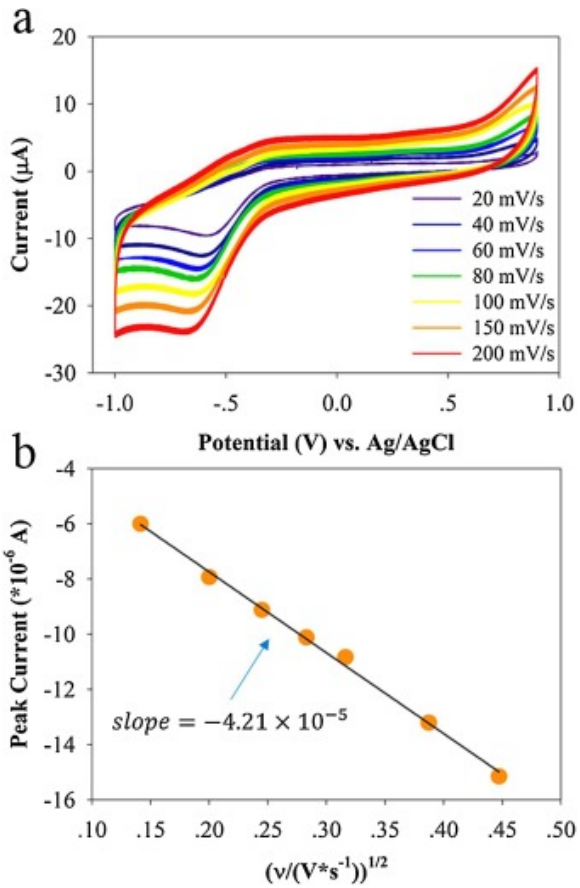

Fig. 4. (a) Representative cyclic voltammograms of the ORR at a bare glassy carbon electrode in O_2 saturated 20 mM KCl electrolyte solution at different scan rates. (b) The linear dependence of the peak current (averaged from three trials) on the square root of the voltage scan rate for the O_2 concentration calculation.

Next the cyclic voltammetric responses of the ECNFs modified electrode and MnO_2/ECNFs (2 h and 4 h) modified electrode were examined by varying the scan rates from 20 mV/s to 200 mV/s, which also show an increase in the cathodic peak current with respect to the scan rate as Fig. 5a and 5b show. In comparison, there is a marked enhancement in the ORR of the electrode

modified with MnO_2/ECNFs (4 h). Note that the anodic peak presented at 0.32 V is attributed to the oxidation reactions between the Mn(IV)/Mn(III) complexes [54]. As mentioned above, Eq. (2) is also used to calculate the number of electrons in the overall electrochemical processes for electrodes modified with super-aligned ECNFs and MnO_2/ECNFs. The peak currents are directly proportional to the square roots of scan rates for both modified electrodes with a slope of -8.01×10^{-5} (ECNFs modified electrode) and -1.59×10^{-4} (MnO_2/ECNFs (4 h) modified electrode), respectively (Fig. 5c). Moreover, the slope of a plot of $\log(i_p)$ (i_p is in unit of A) versus potential (potential is in unit of V) (Fig. 5d) and the following equation is used to determine the transfer coefficient [55]:

$$Slope = \frac{-\alpha F}{2.3RT} \tag{3}$$

where R is the gas constant, F is the Faraday's constant, and T is the temperature. The transfer coefficient is obtained to be 0.65 (ECNFs modified electrode) and 0.52 (MnO_2/ECNFs (4 h) modified electrode), respectively. By using Eq. (2), this value can then be coupled with the active surface area, the diffusion coefficient of oxygen, and the concentration of oxygen to extract the number of electrons exchanged as 2.26 (ECNFs modified electrode) and 3.84 (MnO_2/ECNFs (4 h) modified electrode), respectively. Meanwhile, in comparison, with a transfer coefficient of 0.58 (Fig. 5d) and a slope of -1.39×10^{-4} (Fig. 5c), the number of electrons exchanged is obtained to be 3.37 for the MnO_2/ECNFs (2 h) modified electrode, because the oxygen and hydrogen peroxide are not effectively confined within the imperfectly fiber-covered MnO_2/ECNFs-GC system. As expected, the voltammetric curve of an ECNFs modified electrode exceeds a 2-electron transfer ORR through an energetically favored association to assist the adsorption and reduction of oxygen molecules, which is characteristics of the activity of ECNFs [38], [39]. However, for the MnO_2/ECNFs modified electrode, considering that the hydrogen peroxide molecule generated from the electrochemical reduction of oxygen to be decomposed repeatedly at the surface of a uniform MnO_2 film, a nearly 4-electron pathway presents contributed with cycles of oxygen decomposition/regeneration.

Since the catalytic decomposition of hydrogen peroxide typically follows the first order kinetics [56], to test our hypothesis of hydrogen peroxide decomposition at the surface of a uniform MnO_2 film (4 h), the cyclic voltammogram of a MnO_2/ECNFs modified electrode was studied in an N_2 saturated 20 mM KCl electrolyte solution with 1 mM hydrogen peroxide at different scan rates (Fig. 6a). No measureable reduction peak shows for an ECNFs modified electrode in an N_2 saturated 20 mM KCl electrolyte solution with 1 mM hydrogen peroxide (Fig. S4). However, a marked increase in the voltammetric performance of the MnO_2/ECNFs modified electrode was observed as a result from the electrochemical decomposition of hydrogen peroxide successfully taking place at the electrode surface. This is reasonable agreement with the results reported for the catalytic decomposition of hydrogen peroxide by using hematite [57], cobalt [58], and iron [59]. Furthermore, in the same way, slope of the plot of $\log(i_p)$ versus potential (Fig. 6b inserted) and Eq. (3) were used to determine the transfer coefficient of 0.09. When the constants of active surface area (0.071 cm^2), diffusion coefficient of hydrogen peroxide (reported value of 1.0×10^{-5} cm^2/s)[60] and concentration of hydrogen peroxide (1.0×10^{-6} mol/mL) are applied for the slope obtained from the MnO_2/ECNFs modified electrode (Fig. 6b), a n value of 1.91 is extracted. This highly supports that the hydrogen

peroxide molecules generated from the electrochemical reduction of oxygen are decomposed by the uniform MnO_2 film. The hydrogen peroxide decomposition by the uniform α-MnO_2 film can be ascribed to two reasons: one is the open crystal structure of α-MnO_2 with 2 × 2 tunnels providing favorable surface coordination [61], such as the higher Miller index (211) and (112) surfaces are expressed in the XRD results; and the other is the low oxygen vacancy formation energy providing a favorable thermodynamic pathway for catalytic processes, such as 1.09 eV for (211) and 0.07 eV for (112) [62].

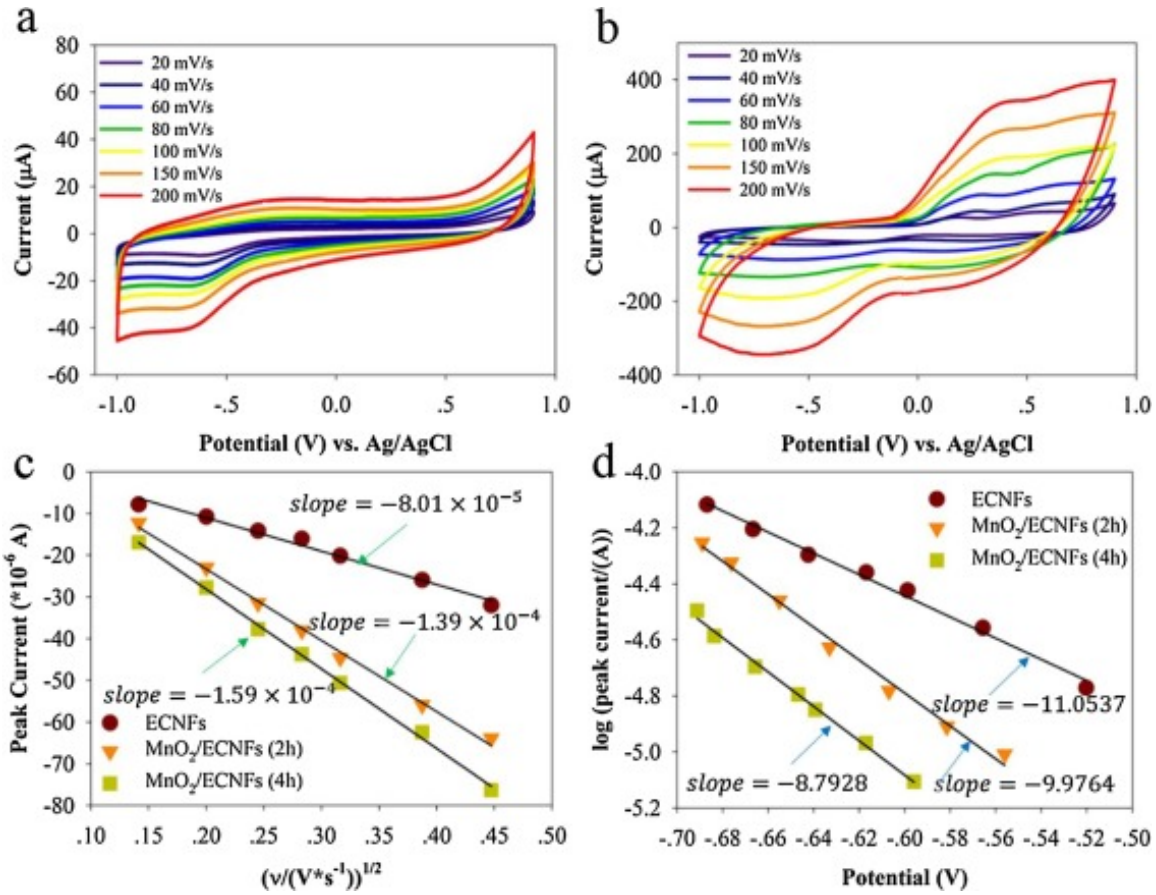

Fig. 5. Cyclic voltammograms of the ORR at the electrode modified with super-aligned ECNFs (a) and MnO_2/ECNFs (4 h) (b) in O_2 saturated 20 mM KCl electrolyte solution at different scan rates. (c) The linear dependence of the peak current on the square root of the scan rate for the number of electrons exchanged calculation. (d) The linear dependence of the log of the peak current on the potential for the transfer coefficient calculation.

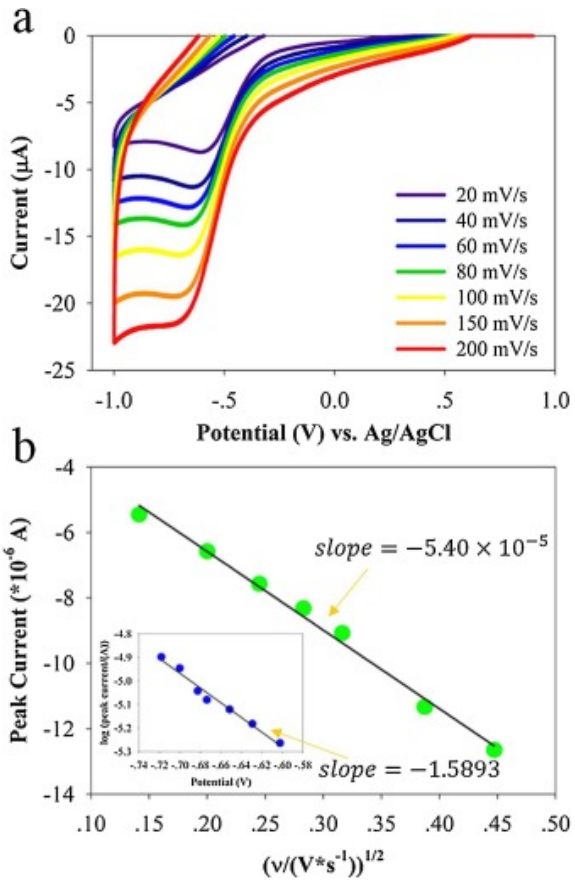

Fig. 6. (a) Representative cyclic voltammograms of the H_2O_2 reduction reaction at the electrode modified with MnO_2/ECNFs (4 h) in N_2 saturated 20 mM KCl electrolyte solution with 1 mM H_2O_2 at different scan rates. (b) The linear dependence of the peak current on the square root of the scan rate for the number of electrons exchanged calculation, inserted with the linear dependence of the log of the peak current on the potential for the transfer coefficient calculation.

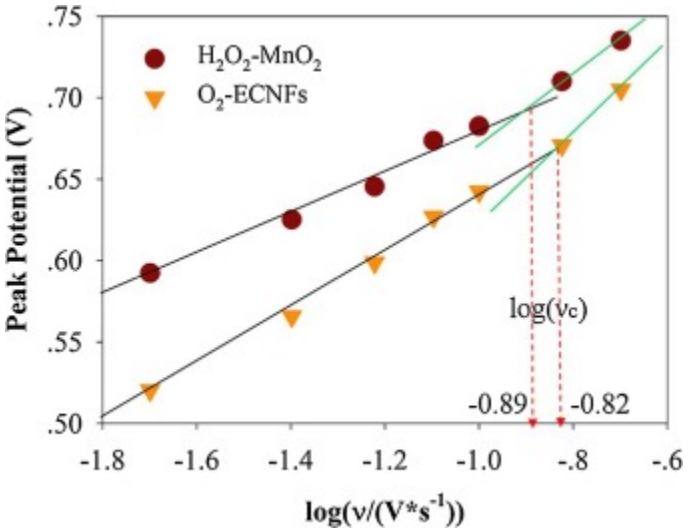

Fig. 7. Plots of peak potential versus log of scan rate for critical scan rate determination under the conditions of H_2O_2-MnO_2 and O_2-ECNFs.

To compare the rate of the hydrogen peroxide generation by ECNFs modified electrodes (O_2-ECNFs) with the hydrogen peroxide decomposition by MnO_2/ECNFs modified electrode (H_2O_2-MnO_2), the electron transfer kinetics should be taken into account. The Gileadi method based upon the determination of critical scan rate (v_c) was further used to evaluate the heterogeneous electron transfer rate constant (k^0). When the experimental results from O_2-ECNFs and H_2O_2-MnO_2 are applied for this analysis, the critical scan rate can be found from the intersection of two lines as Fig. 7 shows. Then the following equation was used to calculate the k^0 (cm/s) [63].

$$\log(k^0) = -0.48\alpha + \log\left[\frac{nF\alpha v_c D_0}{2.303RT}\right]^{1/2} \quad (4)$$

By using this method, associated with the transfer coefficient, number of electron transfer, and diffusion coefficient obtained above, the value of heterogeneous electron transfer rate constant for O_2-ECNFs and H_2O_2-MnO_2 is calculated to be 1.30×10^{-2} cm/s and 1.37×10^{-2} cm/s, respectively. The rate of hydrogen peroxide decomposition by MnO_2/ECNFs modified electrode is faster than the electrochemical generation process by ECNFs modified electrodes, which may be partly ascribed to the presence of K^+ inside the 2 × 2 tunnels of the α-MnO_2 enhancing the electrocatalytical performance of the catalyst [49].

3.3. 4-electron pathway mechanism

From the catalytic activity analysis, a 4-electron pathway mechanism was further proposed as Fig. 8 shows. When the oxygen molecule has been adsorbed onto the MnO_2/ECNF-GC electrode surfaces, the redox between MnO_2 species assists the charge transfer involved in oxygen reduction, and the first step undergos a 2-electron pathway forming hydrogen peroxide (Eq. (5)) [64].

$$O_{2ads} + 2H^+ + 2e^- \rightarrow H_2O_2 \quad (5)$$

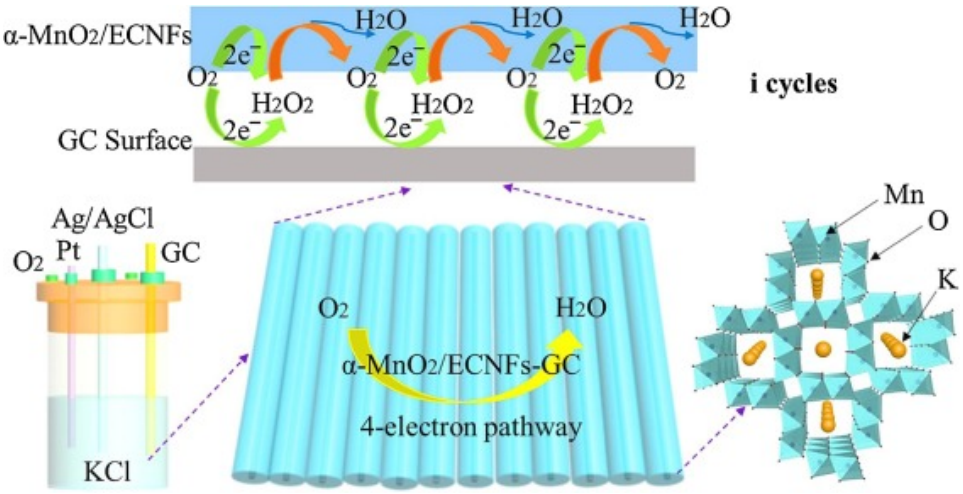

Fig. 8. Illustration of the 4-electron pathway mechanism by the bifunctional catalyst α-MnO_2/ECNFs-GC electrode.

The electrochemically generated hydrogen peroxide can then be decomposed to water via a disproportionation reaction before it escapes into the bulk solution by a uniform α-MnO_2 film (Eq. (6)) [65], though an electrochemical decomposition to OH^- may occur [64].

$$2H_2O_2 \xrightarrow{\alpha-MnO_2} O_2 + 2H_2O \tag{6}$$

The rate of hydrogen peroxide decomposition by α-MnO_2/ECNFs modified electrode is faster than the electrochemical generation process by ECNFs modified electrode, and the presence of K^+ inside the 2 × 2 channels of the α-MnO_2 has a strong beneficial effect on the electrochemical performance of the catalyst [64], which improves the efficiency of the ORR process proved by our results shown above. A half of the oxygen concentration shown in Eq. (6) is electrochemically regenerated after each cycle, which reduces the risk of the fuel cell degradation for practical uses [8].

As a result, Eq. (5) and Eq. (6) occurring in series give the α-MnO_2/ECNF-GC catalytic system as much efficiency as a 4-electron pathway:

$$O_2 + 4H^+ + 4e^- \rightarrow 2H_2O \tag{7}$$

Considering that a cycle of decomposition/regeneration of a half of the oxygen concentration at the MnO_2/ECNF-GC electrode, the contribution for the electron pathway from the bifunctional catalyst can be divided into two parts, i.e. the first 2-electron transfer oxygen reduction to hydrogen peroxide at the GC-MnO_2 interfaces, and following hydrogen peroxide decomposition at the α-MnO_2 surfaces. Fig. 8 shows the proposed reactions where *i* is the number of cycles regarding the reduction of oxygen and regeneration of oxygen with respect to the oxygen and hydrogen peroxide confinement ability. The total number electron pathway can be expressed:

$$N = 2\sum_{i=0}^{\infty}\left(\frac{1}{2}\right)_{GC-MnO_2} + 2\sum_{i=0}^{\infty}\left(\frac{1}{2}\right)_{MnO_2} \tag{8}$$

where *N* is the number-electron pathway, sigma notation is the contribution from different parts, and *i* is the number of cycles regarding the reduction of oxygen and regeneration of oxygen with respect to the oxygen and hydrogen peroxide confinement ability in the aligned MnO_2/ECNFs structures. As the result analysis provided above, the number of electrons exchanged is obtained to be 3.37 (*i* is estimated to be 3) for the 2-hour electrodeposited MnO_2/ECNF electrode (MnO_2 ununiformly covered at ECNFs), because the oxygen and hydrogen peroxide are not completely reduced within the MnO_2/ECNFs-GC system due to the insufficient catalytic activity and confinement (number of cycling). Whereas at 4-hour deposited MnO_2/ECNFs, the number of electrons exchanged is achieved to be 3.84, suggesting a large cycle number (namely good confinement, *i* is estimated to be 5) and excellent catalytic activity are obtained from the uniform electrodeposition of α-MnO_2 on ECNFs.

4. Conclusions

This work demonstrates a new strategy for uniformly electrodepositing α-MnO_2 film on aligned ECNFs and the α-MnO_2 film was well characterized. In contrast to earlier studies with an inhomogeneous surface coverage, the reported α-MnO_2 film with a 4 h–45 μA electrodeposition was uniform with a thickness of 1710 nm. From the electrocatalytic performance studies, the bifunctional catalyst system of α-MnO_2/ECNFs-GC displayed a 3.84-electron pathway through the rapid decomposition of hydrogen peroxide at the α-MnO_2 surfaces. The analysis of electron transfer kinetics suggested a faster hydrogen peroxide decomposition than its generation from reduction of oxygen, and a two-step four-electron pathway cycling mechanism was proposed to give an insightful understanding of the electrocatalytic ORR at the bifunctional catalyst system. These findings represent significant improvement in stable metal oxide/carbonaceous nanomaterial-based oxygen reduction catalysts.

Acknowledgements

This work is supported by NC state fund through the Joint School of Nanoscience and Nanoengineering (JSNN). The authors would like to thank Dr. Lifeng Zhang at North Carolina A&T State University for helping on ECNFs fabrication, and Dr. Brain Bloom in University of Pittsburgh for the XPS test. This work was performed at the JSNN, a member of Southeastern Nanotechnology Infrastructure Corridor (SENIC) and National Nanotechnology Coordinated Infrastructure (NNCI), which is supported by the National Science Foundation (ECCS-1542174).

Appendix A. Supplementary data

Supplementary data associated with this article can be found at https://doi.org/10.1016/j.electacta.2017.10.057.

References

[1] H.A. Gasteiger, S.S. Kocha, B. Sompalli, F.T. Wagner, Activity benchmarks and requirements for Pt, Pt-alloy, and non-Pt oxygen reduction catalysts for PEMFCs, Applied Catalysis B: Environmental 56 (2005) 9–35.

[2] B. Wang, Recent development of non-platinum catalysts for oxygen reduction reaction, Journal of Power Sources 152 (2005) 1–15.

[3] N.E. Sahin, T.W. Napporn, L. Dubau, F. Kadirgan, J.-M. Léger, K.B. Kokoh, Temperature-dependence of oxygen reduction activity on Pt/C and PtCr/C electrocatalysts synthesized from microwave-heated diethylene glycol method, Applied Catalysis B: Environmental 203 (2017) 72–84.

[4] C. Song, Y. Tang, J.L. Zhang, J. Zhang, H. Wang, J. Shen, S. McDermid, J. Li, P. Kozak, PEM fuel cell reaction kinetics in the temperature range of 23–120C, Electrochimica Acta 52 (2007) 2552–2561.

[5] M. Lüsi, H. Erikson, A. Sarapuu, K. Tammeveski, J. Solla-Gullón, J.M. Feliu, Oxygen reduction reaction on carbon-supported palladium nanocubes in alkaline media, Electrochemistry Communications 64 (2016) 9–13.

[6] P. Bocchetta, C.R. Sánchez, A. Taurino, B. Bozzini, Accurate Assessment of the Oxygen Reduction Electrocatalytic Activity of Mn/Polypyrrole Nanocomposites Based on Rotating Disk Electrode Measurements, Complemented with Multitechnique Structural Characterizations, Journal of Analytical Methods in Chemistry (2016) 2016.

[7] R. Baker, D.P. Wilkinson, J. Zhang, Electrocatalytic activity and stability of substituted iron phthalocyanines towards oxygen reduction evaluated at different temperatures, Electrochimica Acta 53 (2008) 6906–6919.

[8] K. Shimizu, L. Sepunaru, R.G. Compton, Innovative catalyst design for the oxygen reduction reaction for fuel cells, Chemical Science 7 (2016) 3364–3369.

[9] H. Sun, G. Zhang, L.-J. Guo, H. Liu, A novel technique for measuring current distributions in PEM fuel cells, Journal of Power Sources 158 (2006) 326–332.

[10] L. Ghassemzadeh, K.-D. Kreuer, J. Maier, K. Müller, Chemical degradation of Nafion membranes under mimic fuel cell conditions as investigated by solid-state NMR spectroscopy, The Journal of Physical Chemistry C 114 (2010) 14635–14645.

[11] S. Zhang, X.-Z. Yuan, J.N.C. Hin, H. Wang, K.A. Friedrich, M. Schulze, A review of platinum-based catalyst layer degradation in proton exchange membrane fuel cells, Journal of Power Sources 194 (2009) 588–600.

[12] S. Freguia, K. Rabaey, Z. Yuan, J. Keller, Non-catalyzed cathodic oxygen reduction at graphite granules in microbial fuel cells, Electrochimica Acta 53 (2007) 598–603.

[13] D. Guo, R. Shibuya, C. Akiba, S. Saji, T. Kondo, J. Nakamura, Active sites of nitrogen-doped carbon materials for oxygen reduction reaction clarified using model catalysts, Science 351 (2016) 361–365.

[14] K. Gong, F. Du, Z. Xia, M. Durstock, L. Dai, Nitrogen-doped carbon nanotube arrays with high electrocatalytic activity for oxygen reduction, Science 323 (2009) 760–764.

[15] N. Marković, P.N. Ross, Surface science studies of model fuel cell electrocatalysts, Surface Science Reports 45 (2002) 117–229.

[16] A. Stassi, C. D'urso, V. Baglio, A. Di Blasi, V. Antonucci, A. Arico, A.C. Luna, A. Bonesi, W. Triaca, Electrocatalytic behaviour for oxygen reduction reaction of small nanostructured crystalline bimetallic Pt–M supported catalysts, Journal of Applied Electrochemistry 36 (2006) 1143–1149.

[17] B. Jiang, C. Li, V. Malgras, M. Imura, S. Tominaka, Y. Yamauchi, Mesoporous Pt nanospheres with designed pore surface as highly active electrocatalyst, Chemical Science 7 (2016) 1575–1581.

[18] C. Li, T. Sato, Y. Yamauchi, Electrochemical Synthesis of One-Dimensional Mesoporous Pt Nanorods Using the Assembly of Surfactant Micelles in Confined Space, Angewandte Chemie 125 (2013) 8208–8211.

[19] W. Chaikittisilp, N.L. Torad, C. Li, M. Imura, N. Suzuki, S. Ishihara, K. Ariga, Y. Yamauchi, Synthesis of Nanoporous Carbon–Cobalt-Oxide Hybrid Electrocatalysts by Thermal Conversion of Metal–Organic Frameworks, Chemistry – A European Journal 20 (2014) 4217–4221.

[20] J. Tang, J. Liu, C. Li, Y. Li, M.O. Tade, S. Dai, Y. Yamauchi, Synthesis of Nitrogen-Doped Mesoporous Carbon Spheres with Extra-Large Pores through Assembly of Diblock Copolymer Micelles, Angewandte Chemie International Edition 54 (2015) 588–593.

[21] S. Mao, Z. Wen, T. Huang, Y. Hou, J. Chen, High-performance bi-functional electrocatalysts of 3D crumpled graphene–cobalt oxide nanohybrids for oxygen reduction and evolution reactions, Energy & Environmental Science 7 (2014) 609–616.

[22] D. Deng, L. Yu, X. Chen, G. Wang, L. Jin, X. Pan, J. Deng, G. Sun, X. Bao, Iron encapsulated within pod-like carbon nanotubes for oxygen reduction reaction, Angewandte Chemie International Edition 52 (2013) 371–375.

[23] G. Chen, J. Sunarso, Y. Zhu, J. Yu, Y. Zhong, W. Zhou, Z. Shao, Highly Active Carbon/a-MnO2 Hybrid Oxygen Reduction Reaction Electrocatalysts, ChemElectroChem 3 (2016) 1760–1767.

[24] M. Sun, Y. Dong, G. Zhang, J. Qu, J. Li, a-Fe 2 O 3 spherical nanocrystals supported on CNTs as efficient non-noble electrocatalysts for the oxygen reduction reaction, Journal of Materials Chemistry A 2 (2014) 13635–13640.

[25] Y. Gorlin, T.F. Jaramillo, A bifunctional nonprecious metal catalyst for oxygen reduction and water oxidation, Journal of the American Chemical Society 132 (2010) 13612–13614.

[26] Y. Meng, W. Song, H. Huang, Z. Ren, S.-Y. Chen, S.L. Suib, Structure–property relationship of bifunctional MnO2 nanostructures: highly efficient, ultra-stable electrochemical water oxidation and oxygen reduction reaction catalysts identified in alkaline media, Journal of the American Chemical Society 136 (2014) 11452–11464.

[27] J.-S. Lee, G.S. Park, H.I. Lee, S.T. Kim, R. Cao, M. Liu, J. Cho, Ketjenblack carbon supported amorphous manganese oxides nanowires as highly efficient electrocatalyst for oxygen reduction reaction in alkaline solutions, Nano letters 11 (2011) 5362–5366.

[28] W. Xiao, D. Wang, X.W. Lou, Shape-controlled synthesis of MnO2 nanostructures with enhanced electrocatalytic activity for oxygen reduction, The Journal of Physical Chemistry C 114 (2009) 1694–1700.

[29] T.N. Lambert, D.J. Davis, W. Lu, S.J. Limmer, P.G. Kotula, A. Thuli, M. Hungate, G. Ruan, Z. Jin, J.M. Tour, Graphene–Ni–a-MnO 2 and –Cu–a-MnO 2 nanowire blends as highly active non-precious metal catalysts for the oxygen reduction reaction, Chemical Communications 48 (2012) 7931–7933.

[30] F. Cheng, T. Zhang, Y. Zhang, J. Du, X. Han, J. Chen, Enhancing electrocatalytic oxygen reduction on MnO2 with vacancies, Angewandte Chemie International Edition 52 (2013) 2474–2477.

[31] T. Zhang, F. Cheng, J. Du, Y. Hu, J. Chen, Efficiently enhancing oxygen reduction electrocatalytic activity of MnO2 using facile hydrogenation, Advanced Energy Materials 5 (2015).

[32] J. Duan, Y. Zheng, S. Chen, Y. Tang, M. Jaroniec, S. Qiao, Mesoporous hybrid material composed of Mn 3 O 4 nanoparticles on nitrogen-doped graphene for highly efficient oxygen reduction reaction, Chemical Communications 49 (2013) 7705–7707.

[33] J.E. Choe, J.-M. You, M. Yun, K. Lee, M.S. Ahmed, Z. Üstundağ, S. Jeon, Manganese dioxide/reduced graphene oxide with poly (3, 4-ethylenedioxythiophene) for improved electrocatalytic oxygen reduction reaction, Journal of Nanoscience and Nanotechnology 15 (2015) 5684–5690.

[34] I. Roche, K. Scott, Carbon-supported manganese oxide nanoparticles as electrocatalysts for oxygen reduction reaction (orr) in neutral solution, Journal of Applied Electrochemistry 39 (2009) 197–204.

[35] D. Liu, X. Zhang, Z. Sun, T. You, Free-standing nitrogen-doped carbon nanofiber films as highly efficient electrocatalysts for oxygen reduction, Nanoscale 5 (2013) 9528–9531.

[36] Z. Zeng, P. Lu, C. Li, L. Mai, Z. Li, Y. Zhang, Removal of NO by carbonaceous materials at room temperature: A review, Catalysis Science & Technology 2 (2012) 2188–2199.

[37] Z. Zeng, Y. Liu, W. Zhang, H. Chevva, J. Wei, Improved supercapacitor performance of MnO 2-electrospun carbon nanofibers electrodes by mT magnetic field, Journal of Power Sources 358 (2017) 22–28.

[38] D. Shin, B. Jeong, B.S. Mun, H. Jeon, H.-J. Shin, J. Baik, J. Lee, On the origin of electrocatalytic oxygen reduction reaction on electrospun nitrogen?carbon species, The Journal of Physical Chemistry C 117 (2013) 11619–11624.

[39] Y. Qiu, J. Yu, T. Shi, X. Zhou, X. Bai, J.Y. Huang, Nitrogen-doped ultrathin carbon nanofibers derived from electrospinning: Large-scale production, unique structure, and

application as electrocatalysts for oxygen reduction, Journal of Power Sources 196 (2011) 9862–9867.

[40] D. Banham, S. Ye, K. Pei, J.-i. Ozaki, T. Kishimoto, Y. Imashiro, A review of the stability and durability of non-precious metal catalysts for the oxygen reduction reaction in proton exchange membrane fuel cells, Journal of Power Sources 285 (2015) 334–348.

[41] W. Zhang, Z. Zeng, J. Wei, Electrochemical study of DPPH radical scavenging for evaluating the antioxidant capacity of carbon nanodots, The Journal of Physical Chemistry C 121 (2017) 18635–18642.

[42] D.P. Dubal, D.S. Dhawale, R.R. Salunkhe, C.D. Lokhande, Conversion of chemically prepared interlocked cubelike Mn3O4 to birnessite MnO2 using electrochemical cycling, Journal of the Electrochemical Society 157 (2010) A812–A817.

[43] Z. Zeng, W. Zhang, D.M. Arvapalli, B. Bloom, A. Sheardy, T. Mabe, Y. Liu, Z. Ji, H. Chevva, D.H. Waldeck, J. Wei, A fluorescence-electrochemical study of carbon nanodots (CNDs) in bio- and photoelectronic applications and energy gap investigation, Physical Chemistry Chemical Physics 19 (2017) 20101–20109.

[44] S.W. Lee, J. Kim, S. Chen, P.T. Hammond, Y. Shao-Horn, Carbon nanotube/manganese oxide ultrathin film electrodes for electrochemical capacitors, ACS nano 4 (2010) 3889–3896.

[45] L. Yuan, X.-H. Lu, X. Xiao, T. Zhai, J. Dai, F. Zhang, B. Hu, X. Wang, L. Gong, J. Chen, Flexible solid-state supercapacitors based on carbon nanoparticles/MnO2 nanorods hybrid structure, ACS nano 6 (2011) 656–661.

[46] P. Yu, X. Zhang, D. Wang, L. Wang, Y. Ma, Shape-controlled synthesis of 3D hierarchical MnO2 nanostructures for electrochemical supercapacitors, Crystal Growth and Design 9 (2008) 528–533.

[47] S. Devaraj, N. Munichandraiah, High capacitance of electrodeposited MnO2 by the effect of a surface-active agent, Electrochemical and Solid-State Letters 8 (2005) A373–A377.

[48] T. Gao, H. Fjellvåg, P. Norby, A comparison study on Raman scattering properties of a-and b-MnO 2, Analytica chimica acta 648 (2009) 235–239.

[49] Y. Yuan, C. Zhan, K. He, H. Chen, W. Yao, S. Sharifi-Asl, B. Song, Z. Yang, A. Nie, X. Luo, The influence of large cations on the electrochemical properties of tunnel-structured metal oxides, Nature Communications 7 (2016) 13374.

[50] H. Muhammad, I.A. Tahiri, M. Muhammad, Z. Masood, M.A. Versiani, O. Khaliq, M. Latif, M. Hanif, A comprehensive heterogeneous electron transfer rate constant evaluation of dissolved oxygen in DMSO at glassy carbon electrode measured by different electrochemical methods, Journal of Electroanalytical Chemistry 775 (2016) 157–162.

[51] R. Nissim, R.G. Compton, Nonenzymatic Electrochemical Superoxide Sensor, ChemElectroChem 1 (2014) 763–771.

[52] L.K. Ju, C.S. Ho, Measuring oxygen diffusion coefficients with polarographic oxygen electrodes: I. electrolyte solutions, Biotechnology and Bioengineering 27 (1985) 1495–1499.

[53] K. Sundberg, W. Smyrl, L. Atanasoska, R. Atanasoski, Surface modification and oxygen reduction on glassy carbon in chloride media, Journal of The Electrochemical Society 136 (1989) 434–439.

[54] M. Toupin, T. Brousse, D. Bélanger, Charge storage mechanism of MnO2 electrode used in aqueous electrochemical capacitor, Chemistry of Materials 16 (2004) 3184–3190.

[55] J. Wang, Analytical electrochemistry, John Wiley & Sons, 2006.

[56] H.-H. Huang, M.-C. Lu, J.-N. Chen, Catalytic decomposition of hydrogen peroxide and 2-chlorophenol with iron oxides, Water Research 35 (2001) 2291–2299.

[57] M. Sun, G. Zhang, H. Liu, Y. Liu, J. Li, a-and g-Fe2O3 nanoparticle/nitrogen doped carbon nanotube catalysts for high-performance oxygen reduction reaction, Science China Materials 58 (2015) 683–692.

[58] Y. Su, Y. Zhu, X. Yang, J. Shen, J. Lu, X. Zhang, J. Chen, C. Li, A highly efficient catalyst toward oxygen reduction reaction in neutral media for microbial fuel cells, Industrial & Engineering Chemistry Research 52 (2013) 6076–6082.

[59] P. Chen, T. Zhou, L. Xing, K. Xu, Y. Tong, H. Xie, L. Zhang, W. Yan, W. Chu, C. Wu, Atomically Dispersed Iron–Nitrogen Species as Electrocatalysts for Bifunctional Oxygen Evolution and Reduction Reactions, Angewandte Chemie International Edition 56 (2017) 610–614.

[60] I. Katsounaros, W.B. Schneider, J.C. Meier, U. Benedikt, P.U. Biedermann, A.A. Auer, K.J. Mayrhofer, Hydrogen peroxide electrochemistry on platinum: towards understanding the oxygen reduction reaction mechanism, Physical Chemistry Chemical Physics 14 (2012) 7384–7391.

[61] V. Giordani, S. Freunberger, P. Bruce, J.-M. Tarascon, D. Larcher, H2O2 decomposition reaction as selecting tool for catalysts in Li–O2 cells, Electrochemical and Solid-state Letters 13 (2010) A180–A183.

[62] D.A. Tompsett, S.C. Parker, M.S. Islam, Surface properties of a-MnO 2: relevance to catalytic and supercapacitor behaviour, Journal of Materials Chemistry A 2 (2014) 15509–15518.

[63] U. Eisner, E. Gileadi, Anodic oxidation of hydrazine and its derivatives: Part I. The oxidation of hydrazine on gold electrodes in acid solutions, Journal of Electroanalytical Chemistry and Interfacial Electrochemistry 28 (1970) 81–92.

[64] F. Cheng, Y. Su, J. Liang, Z. Tao, J. Chen, MnO2-Based Nanostructures as Catalysts for Electrochemical Oxygen Reduction in Alkaline Media, Chemistry of Materials 22 (2010) 898–905.

[65] L. Mao, D. Zhang, T. Sotomura, K. Nakatsu, N. Koshiba, T. Ohsaka, Mechanistic study of the reduction of oxygen in air electrode with manganese oxides as electrocatalysts, Electrochimica Acta 48 (2003) 1015–1021.